Vortex penalization method for bluff body flows

Federico Gallizio, Chloé Mimeau, Georges-Henri Cottet, Iraj Mortazavi

Vortex penalization method for bluff body flows

F. Gallizio, C. Mimeau, G.-H. Cottet, I. Mortazavi

In this work a penalization method is discussed in the context of vortex methods for incompressible flows around complex geometries. We in particular illustrate the method in two cases : the flow around a rotating blade for Reynolds Numbers 1000 and 10000 and the flow past a semi-circular body consisting of a porous layer surrounding a rigid body at Reynolds numbers 550 and 3000. In the latter example, the results are interpreted in terms of control strategy.

1 Introduction

Vorticity is an important characteristic of flows in many applications. It is a signature of wakes in bluff body flows and, as such, is related to aerodynamic performance of moving or fixed obstacles [39]. The vorticity formulation of the Navier-Stokes equations is therefore a natural framework to address questions related to flow control. In these equations, for moderate and high Reynolds number the vorticity advection is predominant, which motivates the use of Lagrangian or semi Lagrangian schemes to discretize these equations. Particle methods belong to this category. They have long been used for the simulation of vortex flows, and in particular for bluff body flows, since the pioneering simulation of flows past a 2D cylinder in [24]. Three dimensional simulations followed this work [30, 17, 31]. In all these works the no-slip condition at the body surface is imposed through vorticity fluxes. This method relies on an analysis of the relationship between vorticity fluxes and velocity boundary conditions [16, 17]. Vorticity fluxes are implemented in vortex methods by means of integral equations [25]. This method is physically appealing but relies on a delicate tuning of several parameters and remains delicate to implement. Immersed boundary conditions have been proposed in [29, 17] to simplify the treatment of complex geometry and the computation of velocity from vorticity. Later on, following the work of [1, 23], a penalization method coupled to the vorticity formulation of the Navier-Stokes equation was proposed and extended to the two-way interaction of a rigid body and a three-dimensional incompressible fluid in [15]. The method was validated in three dimensional flows at low Reynolds numbers. The work in [33] provides additional 2D validations of the method and illustrates its efficiency in the context of GPU computing.

The purpose of this paper is to further illustrate the flexibility of this method by focusing on the case of two bi-dimensional complex flows : the flow around a vertical axis turbine (VAT), on the one hand, and the flow past a semi-circular obstacle made of a porous layer surrounding a rigid core, on the second hand. In the first case, we discuss the different flow patterns and frequencies corresponding to moderate and high Reynolds numbers. In the second case we study the influence of the porous layer on the wake strength and on the drag value.

This paper is organized as follows. In section 2 we describe the vortex penalization model and its implementation in a vortex particle method. In particular, we indicate how the body forces are computed in such a model. In section 3 we first validate the method on the benchmark test of the flow past a 2D circular cylinder at various Reynolds numbers, and then apply the

method to the case of a rotating turbine blade. Section 4 is devoted to the analysis of the flow around a semi-circular cylinder with a porous coating. The characteristics of the flows are analyzed from the point of view of flow control. Finally section 5 summarizes our results and draws some conclusions.

2 Numerical algorithm

2.1 Vorticity formulation and remeshed particle method

The dynamics of an incompressible flow is governed by the incompressible Navier-Stokes equations :

$$\boldsymbol{\nabla} \cdot \mathbf{u} = 0 \quad \text{in } D \tag{1}$$

$$\frac{\partial \mathbf{u}}{\partial t} + (\mathbf{u} \cdot \boldsymbol{\nabla})\mathbf{u} = -\boldsymbol{\nabla} p + \frac{1}{\mathrm{Re}} \boldsymbol{\Delta} \mathbf{u} \quad \text{in } D, \tag{2}$$

where D is the computational domain and Re is the Reynolds number.

Taking the curl of equation (2) and using equation (1), we get the Helmholtz or the Vorticity Transport Equation (VTE) for the vorticity $\boldsymbol{\omega} = \boldsymbol{\nabla} \times \mathbf{u}$:

$$\frac{\partial \boldsymbol{\omega}}{\partial t} + (\mathbf{u} \cdot \boldsymbol{\nabla})\boldsymbol{\omega} - (\boldsymbol{\omega} \cdot \boldsymbol{\nabla})\mathbf{u} = \frac{1}{\mathrm{Re}} \boldsymbol{\Delta} \boldsymbol{\omega} \quad \text{in } D, \tag{3}$$

This equation has to be coupled to the system giving the velocity in terms of the vorticity. It is convenient to use the Helmholtz decomposition :

$$\mathbf{u} = \boldsymbol{\nabla} \times \boldsymbol{\psi} + \boldsymbol{\nabla} \varphi. \tag{4}$$

The stream function $\boldsymbol{\psi}$ and potential φ satisfy the following systems in D :

$$-\boldsymbol{\Delta} \boldsymbol{\psi} = \boldsymbol{\omega}, \ \boldsymbol{\nabla} \cdot \boldsymbol{\psi} = 0, \ \boldsymbol{\Delta} \varphi = 0, \tag{5}$$

complemented with appropriate boundary conditions. The VTE does not explicitly contain the pressure term but the pressure can be recovered from the velocity field by integrating the following Poisson equation :

$$\boldsymbol{\Delta} p = \boldsymbol{\nabla} \cdot (\mathbf{u} \cdot \boldsymbol{\nabla})\mathbf{u}, \quad \text{in } D, \tag{6}$$

which is derived as the divergence of equation (2).

The previous equations are approximated using a vortex particle method [13], [16]. In this approach, the vorticity is carried by particles. Particles follow the trajectories associated to the velocity field. Simultaneously the vorticity carried by the particles is updated to account for vortex stretching and diffusion. In the present work we use particle remeshing to overcome accuracy loss due to local distortion of the flow map. In that case, particles are remeshed through interpolation on a regular mesh at each time step. This grid is used to compute the velocity through a Poisson solver. Details of the algorithm are given in the sequel.

In incompressible flows, the unique sources of the vorticity are boundaries. It is therefore important to capture in an accurate way vorticity boundary conditions. In classical implementations of vortex methods, the no-slip boundary condition is satisfied through the creation of vortex elements [13, 14, 19] or by updating particle strength to account for vorticity fluxes at the boundary [25, 17]. The no-through flow boundary conditions is implemented together with the Poisson equation to determine stream functions and potential in (5).

These methods involve several parameters to enforce the no-slip conditions at the boundaries : a more straightforward alternative to these techniques can be derived from the penalization method.

2.2 Vortex penalization method

2.2.1 Penalization in velocity formulation

In this section we show how the penalization method can be used successfully to model the flow of an incompressible fluid around an obstacle. In the penalization technique the system is considered as a single flow, subject to the Navier-Stokes equation with a penalization term that enforces continuity at the solid-fluid interface and rigid motion inside the solid. The main advantage of this method is that it needs neither the mesh to fit the boundaries nor to specify no-slip boundary conditions. In addition it allows to compute the pressure as a continuous field on the whole domain including the solids, and the lift and drag coefficients by integrating the penalization term inside the solid bodies [11].
In a porous medium the velocity $\mathbf{u}$ is given by the Darcy law :

$$\mathbf{u} = -\frac{k}{\mu\Phi}\boldsymbol{\nabla} p, \tag{7}$$

where p is the pressure, k is the intrinsic permeability, μ is the dynamic viscosity of the fluid and Φ is the porosity of the medium. Assuming that the Boussinesq hypothesis is satisfied for the fluid saturating the porous medium, we get from Brinkman's equation that is valid only for high porosities close to one

$$\boldsymbol{\nabla} p = -\frac{\mu}{k}\Phi\mathbf{u} + \tilde{\mu}\Phi\boldsymbol{\Delta}\mathbf{u} \tag{8}$$

by adding the inertial terms with the Dupuit-Forchheimer relationship [27], the Forchheimer-Navier-Stokes equations

$$\rho\,\partial_t\mathbf{u} + \rho\,(\mathbf{u}\cdot\boldsymbol{\nabla})\,\mathbf{u} + \boldsymbol{\nabla} p = -\frac{\mu}{k}\Phi\mathbf{u} + \tilde{\mu}\Phi\boldsymbol{\Delta}\mathbf{u}, \tag{9}$$

where ρ is the density of the fluid and $\tilde{\mu}$ is Brinkman's effective viscosity. As Φ is close to 1 we can approximate $\tilde{\mu} \approx \frac{\mu}{\Phi}$ [38] and get the equation :

$$\rho\,\partial_t\mathbf{u} + \rho\,(\mathbf{u}\cdot\boldsymbol{\nabla})\,\mathbf{u} + \boldsymbol{\nabla} p = -\frac{\mu}{k}\Phi\mathbf{u} + \mu\boldsymbol{\Delta}\mathbf{u}. \tag{10}$$

Then a non-dimensionalization using the usual substitutions including the mean velocity of the fluid $\overline{\mathbf{u}}$ and the size if the body H

$$\mathbf{u} = \mathbf{u}'\,\overline{\mathbf{u}}\ ;\ \ x = x'\,H\ ;\ \ t = t'\frac{H}{\overline{\mathbf{u}}}\ ;\ \ p = p'\rho|\overline{\mathbf{u}}|^2 \tag{11}$$

yields the penalized non dimensional Navier-Stokes equations or Brinkman-Navier-Stokes equations for the unknowns $(\mathbf{u}', p')$ denoted $(\mathbf{u}, p)$ for the sake of simplicity :

$$\partial_t\mathbf{u} + (\mathbf{u}\cdot\boldsymbol{\nabla})\mathbf{u} - \frac{1}{\mathrm{Re}}\boldsymbol{\Delta}\mathbf{u} + \frac{\mathbf{u}}{K} + \boldsymbol{\nabla} p = 0 \quad \text{in } D_T = D\times(0,T) \tag{12}$$

$$\mathrm{div}\,\mathbf{u} = 0 \quad \text{in } D_T, \tag{13}$$

where $K = \frac{\rho k\overline{\mathbf{u}}}{\mu H\Phi}$ is the non dimensional coefficient of permeability of the medium, $\mathrm{Re} = \frac{\rho\overline{\mathbf{u}}H}{\mu}$ is the Reynolds number based on H the height of the body and D the full domain including the solid body. This model is able to represent the two media as follows. The zone variation is realized changing the penalization coefficient that defines the permeability of each region. In the fluid the permeability coefficient goes to infinity, the penalization term vanishes and we solve

the non dimensional Navier-Stokes equations. In the solid body the permeability coefficient goes to zero and it has been shown in [1] that solving these equations corresponds to solve Darcy's law in the solid and that the velocity is proportional to K. One can thus write $K = \frac{1}{\lambda}\chi_S$ where χ_S denotes the characteristic function of S and λ is a penalization parameter satisfying $\lambda \gg 1$. For numerical simulations we typically set $\lambda \geq 10^8$. If the full domain including the solid body is defined as $D = F \cup S$, one finally obtains the following penalized Navier-Stokes equations :

$$\partial_t \mathbf{u} + (\mathbf{u}\cdot\boldsymbol{\nabla})\mathbf{u} - \frac{1}{\mathrm{Re}}\boldsymbol{\Delta}\mathbf{u} + \lambda\chi_S\mathbf{u} + \boldsymbol{\nabla}p \quad = 0 \ \text{ in } \ D \tag{14}$$

$$\mathrm{div}\ \mathbf{u} \quad = 0 \ \text{ in } \ D. \tag{15}$$

In addition as the pressure is computed inside the solid body, it is shown in [11] that one can compute the drag and lift forces by integrating the penalization term on the volume of the body :

$$\mathbf{F} = -\frac{1}{\mathrm{Re}}\int_S \boldsymbol{\Delta}\mathbf{u}\ d\mathbf{x} + \int_S \boldsymbol{\nabla}p\ d\mathbf{x} \ \approx \int_D \lambda\,\chi_S\,\mathbf{u}\ d\mathbf{x}, \tag{16}$$

where the body includes the porous layers.

2.2.2 Penalization in vorticity formulation and implementation with a vortex method

We first show how to extend the penalization method to the vorticity formulation of the Navier-Stokes equations.

By differentiation of the velocity based penalization equation (14), we obtain the following non dimensional [23, 15] vorticity-penalization equation :

$$\frac{\partial\boldsymbol{\omega}}{\partial t} + (\mathbf{u}\cdot\boldsymbol{\nabla})\boldsymbol{\omega} - (\boldsymbol{\omega}\cdot\boldsymbol{\nabla})\mathbf{u} = \frac{1}{\mathrm{Re}}\boldsymbol{\Delta}\boldsymbol{\omega} + \boldsymbol{\nabla}\times[\lambda\ \chi_S(\mathbf{u}_s - \mathbf{u})]. \tag{17}$$

In the above equation we have generalized the boundary value problem to allow for a rigid body motion of the obstacle S with velocity $\mathbf{u}_s$, where $\mathbf{u}_s$ is the rigid body velocity and χ_S is the characteristic function of the solid. This system has to be complemented by the usual system giving the velocity in terms of the vorticity :

$$\boldsymbol{\nabla}\cdot\mathbf{u} = 0 \text{ in } D; \qquad \boldsymbol{\nabla}\times\mathbf{u} = \boldsymbol{\omega} \text{ in } D \tag{18}$$

and appropriate boundary conditions on the walls Γ_D.

We describe here how the vorticity equation (17) is discretized in a vortex method. For simplicity we assume that the computational domain, including the solid body, is covered by a uniform Cartesian grid with mesh-size h.

The equation (17) is split in two sub-steps. At each time step, one successively solves the following equations :

$$\frac{\partial\boldsymbol{\omega}}{\partial t} = \boldsymbol{\nabla}\times(\lambda\ \chi_S(\mathbf{u}_s - \mathbf{u})) \tag{19}$$

$$\frac{\partial\boldsymbol{\omega}}{\partial t} + (\mathbf{u}\cdot\boldsymbol{\nabla})\,\boldsymbol{\omega} - (\boldsymbol{\omega}\cdot\boldsymbol{\nabla})\mathbf{u} = \frac{1}{\mathrm{Re}}\boldsymbol{\Delta}\boldsymbol{\omega}. \tag{20}$$

We set $t_n = n\Delta t$, where Δt is the time-step. If $\mathbf{u}^n, \boldsymbol{\omega}^n$ denote velocity and vorticity values on the grid at time t_n, following [15] the resolution of equation (19) is performed using an Euler implicit scheme, which yields :

$$\widetilde{\boldsymbol{\omega}}^{n+1} = \boldsymbol{\nabla} \times \left[\frac{\mathbf{u}^n + \lambda \Delta t \chi_S \mathbf{u}_s^n}{1 + \lambda \Delta t \chi_S} \right]. \tag{21}$$

The right hand side above is evaluated by centered finite differences on the grid.

To solve the advection-stretching-diffusion equation (20), we proceed as follows. Particles are initialized on grid points where vorticity value is above a given threshold (typically 10^{-5}). If $\mathbf{x}_p^n, \boldsymbol{\omega}_p^n$ denote the locations (grid points) and vorticity of particles ($\boldsymbol{\omega}_p^n = \widetilde{\boldsymbol{\omega}}^{n+1}(\mathbf{x}_p)$), the equation (20) is firstly handled by solving the following system of ODEs [16] :

$$d\mathbf{x}_p/dt = \mathbf{u}_p \ , \ d\boldsymbol{\omega}_p/dt = [\boldsymbol{\nabla} \mathbf{u}_p]\boldsymbol{\omega}_p. \tag{22}$$

This system is typically solved using a second order Runge-Kutta time-stepping. Let us denote by $\mathbf{x}_p^{n+1}, \widetilde{\boldsymbol{\omega}}_p^{n+1}$ the locations and strengths of the particle at the end of the time step. Particles are then remeshed on the original grid points by interpolation, with the formula :

$$\boldsymbol{\omega}_p^{n+1} = \sum_p \widetilde{\boldsymbol{\omega}}_p^{n+1} \Lambda \left(\frac{\mathbf{x}_p^n - \mathbf{x}_p^{n+1}}{h} \right). \tag{23}$$

The function Λ in the above formula is obtained by tensor product from the following piecewise cubic third order interpolation kernel [16] :

$$\Lambda(x) = \begin{cases} 0 & \text{if } |x| > 2 \\ \frac{1}{2}(2 - |x|)^2(1 - |x|) & \text{if } 1 \leq |x| \leq 2 \\ 1 - \frac{5x^2}{2} + \frac{3|x|^3}{2} & \text{if } |x| \leq 1 \end{cases} \tag{24}$$

The same kernel is used to interpolate grid velocity values onto particles in the RK2 time-stepping scheme to solve (22).

After remeshing, vorticity values are known on the grid and the remaining diffusion equation is implicitly solved either with a grid-based Poisson solver or with a Fourier method. Grid values for the vorticity are now available for time t_{n+1}. Velocity values are in turn obtained from vorticity grid values by solving the system (4,5) with a classical grid-based Poisson solver or using a Fourier method, and a new cycle of iterations can start.

One of the main feature of particle methods is that they do not have a CFL restriction on the time step Δt. It is indeed shown in [18] that a remeshed particle method for a transport equation with velocity $\mathbf{u}$ is stable under the condition

$$\Delta t \leq \frac{C}{\|\nabla \mathbf{u}\|_\infty}, \tag{25}$$

where C is a constant that only needs to be smaller than 1.

2.3 Force calculation

Assume a flow in $\mathbb{R}^N$ around a bounded body S with velocity and vorticity vanishing at infinity and having a prescribed value $\mathbf{u}_b$ on the body. The force evaluation given in the formula (16) assumes that the velocity is of the order of K inside the body. This is verified if

the penalization method is used in a velocity-pressure formulation. In a vorticity formulation however, there is no direct control of the velocity in the body. In practice one observes that the velocity in the body is small but larger than K. This can be seen in figure 2(left). In that case, one must go back to force evaluations in terms of vorticity distributions around the body.

The force $\mathcal{F}$ exerted by this flow on the body is given by the following formula :

$$\mathcal{F} = -\frac{d}{dt}\int_{S'} \mathbf{u}\, d\mathbf{x}, \tag{26}$$

where S' denotes the domain outside S. Integration by parts allows to express this force in terms of the vorticity, with N denoting the space dimension :

$$\mathcal{F} = -\frac{1}{N-1}\frac{d}{dt}\int_{S'} \mathbf{x}\times\boldsymbol{\omega}\, d\mathbf{x} - \frac{1}{N-1}\frac{d}{dt}\oint_{\partial S} \mathbf{x}\times(\mathbf{n}\times\mathbf{u}) d\mathbf{s}, \tag{27}$$

where the first integral is the linear hydrodynamical impulse and the second integral is the bound vorticity (see [36]). For an impulsively started obstacle at early times, the vorticity remains essentially attached to the body, and this formula can be used by taking a computational domain large enough to contain the vorticity support. When vorticity shedding occurs, this is no longer possible. Alternatively, one may use the Navier-Stokes equations and the expression (26) to obtain :

$$\mathcal{F} = -\nu\int_{\partial S} \boldsymbol{\omega}\times\mathbf{n}\, d\mathbf{s} + \int_{\partial S} p\cdot\boldsymbol{\omega}\, d\mathbf{s}. \tag{28}$$

In the case of a 2D circular cylinder of radius R, this yields the following formula [24] :

$$\mathcal{F} = \nu R\left(\int_0^{2\pi} \omega\overrightarrow{\mathbf{e}_\theta}\, d\theta - \int_0^{2\pi}\frac{\partial\omega}{\partial n}\overrightarrow{\mathbf{e}_\theta}\, d\theta\right). \tag{29}$$

This expression assumes that vorticity vanishes at infinity, which in practice is always the case, and allows to distinguish friction (in the first integral) and pressure drag (in the second integral).

For a detached bluff body flow this formula can be used as long as vorticity and its normal derivatives are accurately captured at the boundary. However, the penalization method just described is derived from a method which is only first order for the velocity. It therefore does not capture vorticity values and fluxes at the boundary with enough accuracy to give reliable force evaluation through (29) with reasonable grid sizes. It is therefore necessary to use a third technique which combines time derivatives, volumes integral of the vorticity momentum - like in formula (27) - and vorticity boundary values as well as fluxes on a surface away from the body, where these quantities are accurately computed. We follow the approach proposed in [28], and rewrite the force according to the *momentum equation* as follows :

$$\mathcal{F} = -\frac{d}{dt}\int_V \mathbf{u}\, d\mathbf{x} + \int_\Sigma \mathbf{n}\cdot\boldsymbol{\gamma}\, d\mathbf{x}, \tag{30}$$

where V is a domain containing S, Σ denotes its boundary and

$$\begin{aligned}\boldsymbol{\gamma} = & \\ &\frac{1}{2}|\mathbf{u}|^2\mathbf{I} - \frac{1}{N-1}\mathbf{u}\cdot(\mathbf{x}\times\boldsymbol{\omega}) + \frac{1}{N-1}\boldsymbol{\omega}\cdot(\mathbf{x}\times\mathbf{u}) \\ &-\frac{1}{N-1}\left[\left(\mathbf{x}\cdot\frac{\partial\mathbf{u}}{\partial t}\right)\mathbf{I} - \mathbf{x}\cdot\frac{\partial\mathbf{u}}{\partial t}\right] + \frac{1}{N-1}\left[\mathbf{x}\cdot(\boldsymbol{\nabla}\cdot\mathcal{T})\mathbf{I} - \mathbf{x}(\boldsymbol{\nabla}\cdot\mathcal{T})\right] + \mathcal{T}.\end{aligned} \tag{31}$$

In the above equation $\mathcal{T}$ denotes the stress tensor :

$$\mathcal{T} = \mu(\boldsymbol{\nabla}\mathbf{u} + \boldsymbol{\nabla}\mathbf{u}^{\mathbf{t}}), \tag{32}$$

where μ is the viscosity. For a sake of simplicity we develop this formula in the two-dimensional case where the computational box D and the volume control V are two nested rectangles. We use the notations given in figure 1. We denote the velocity by $\mathbf{u} = (u, v)^{\mathbf{t}}$. The streamwise and

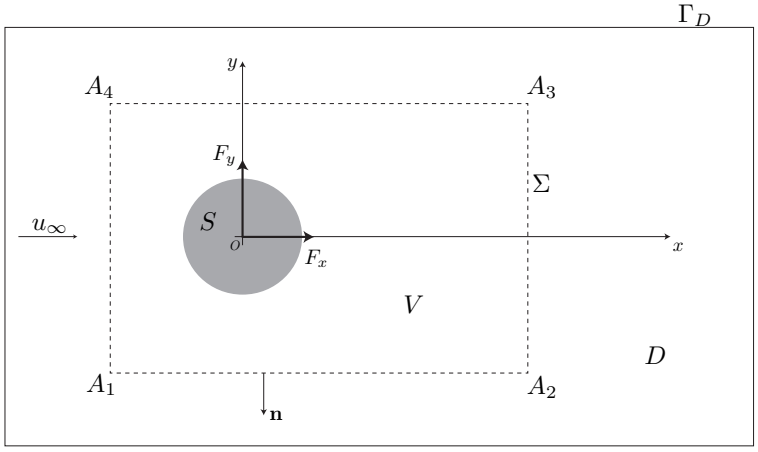

FIGURE 1 – Computational domain D and control volume V.

vertical components of the force can then be written computed as :

$$\begin{aligned}
\mathcal{F}_x = &-\frac{d}{dt}\int_V u(1-\chi_S)\,dxdy \\
&+\int_{A_1}^{A_2}\left[uv + v\omega y - y\frac{\partial u}{\partial t} + \frac{1}{\mathrm{Re}}\left(2\frac{\partial^2 u}{\partial x^2} + \frac{\partial^2 u}{\partial y^2} + \frac{\partial^2 v}{\partial x \partial y}\right)y - \frac{1}{\mathrm{Re}}\left(\frac{\partial u}{\partial y} + \frac{\partial v}{\partial x}\right)\right]dx \\
&+\int_{A_2}^{A_3}\left[\frac{1}{2}(v^2-u^2) - u\omega y - y\frac{\partial v}{\partial t} + \frac{1}{\mathrm{Re}}\left(2\frac{\partial^2 v}{\partial y^2} + \frac{\partial^2 v}{\partial x^2} + \frac{\partial^2 u}{\partial x \partial y}\right)y + \frac{2}{\mathrm{Re}}\left(\frac{\partial u}{\partial x}\right)\right]dy \\
&+\int_{A_3}^{A_4}\left[-uv - v\omega y + y\frac{\partial u}{\partial t} - \frac{1}{\mathrm{Re}}\left(2\frac{\partial^2 u}{\partial x^2} + \frac{\partial^2 u}{\partial y^2} + \frac{\partial^2 v}{\partial x \partial y}\right)y + \frac{1}{\mathrm{Re}}\left(\frac{\partial u}{\partial y} + \frac{\partial v}{\partial x}\right)\right]dx \\
&+\int_{A_4}^{A_1}\left[-\frac{1}{2}(v^2-u^2) + u\omega y + y\frac{\partial v}{\partial t} - \frac{1}{\mathrm{Re}}\left(2\frac{\partial^2 v}{\partial y^2} + \frac{\partial^2 v}{\partial x^2} + \frac{\partial^2 u}{\partial x \partial y}\right)y - \frac{2}{\mathrm{Re}}\left(\frac{\partial u}{\partial x}\right)\right]dy,
\end{aligned}$$

and

$$
\begin{aligned}
\mathcal{F}_y = & -\frac{d}{dt}\int_V v(1-\chi_S)\,dxdy \\
& + \int_{A_1}^{A_2}\left[\frac{1}{2}(v^2-u^2) - v\omega x + x\frac{\partial u}{\partial t} - \frac{1}{\mathrm{Re}}\left(2\frac{\partial^2 u}{\partial x^2} + \frac{\partial^2 u}{\partial y^2} + \frac{\partial^2 v}{\partial x \partial y}\right)x - \frac{2}{\mathrm{Re}}\left(\frac{\partial v}{\partial y}\right)\right] dx \\
& + \int_{A_2}^{A_3}\left[-uv + u\omega x + x\frac{\partial v}{\partial t} - \frac{1}{\mathrm{Re}}\left(2\frac{\partial^2 v}{\partial y^2} + \frac{\partial^2 v}{\partial x^2} + \frac{\partial^2 u}{\partial x \partial y}\right)x + \frac{1}{\mathrm{Re}}\left(\frac{\partial v}{\partial x} + \frac{\partial u}{\partial y}\right)\right] dy \\
& + \int_{A_3}^{A_4}\left[-\frac{1}{2}(v^2-u^2) + v\omega x - x\frac{\partial u}{\partial t} + \frac{1}{\mathrm{Re}}\left(2\frac{\partial^2 u}{\partial x^2} + \frac{\partial^2 u}{\partial y^2} + \frac{\partial^2 v}{\partial x \partial y}\right)x + \frac{2}{\mathrm{Re}}\left(\frac{\partial v}{\partial y}\right)\right] dx \\
& + \int_{A_4}^{A_1}\left[uv - u\omega x - x\frac{\partial v}{\partial t} + \frac{1}{\mathrm{Re}}\left(2\frac{\partial^2 v}{\partial y^2} + \frac{\partial^2 v}{\partial x^2} + \frac{\partial^2 u}{\partial x \partial y}\right)x - \frac{1}{\mathrm{Re}}\left(\frac{\partial v}{\partial x} + \frac{\partial u}{\partial y}\right)\right] dy.
\end{aligned}
$$

For a two dimensional viscous flow past a circular obstacle of diameter d with free stream velocity u_∞, drag and lift coefficients are expressed by the following formulas :

$$
C_D = \frac{2\mathcal{F}_x}{\rho u_\infty^2 d}, \qquad C_L = \frac{2\mathcal{F}_y}{\rho u_\infty^2 d}. \tag{33}
$$

3 Validation and numerical results

The vortex penalization has been validated in 2D and 3D fluid structure interaction problems at low Reynolds numbers [15], in the context of multi-resolution [32] and in GPU implementations for 2D cases [33]. In this section, our goal is to take advantage of the flexibility of the vortex penalization method to handle moving or complex bodies. To evaluate the accuracy of the method, in particular with respect to the value of the penalization parameter, we start with validations on the classical benchmark of the flow around a two-dimensional circular cylinder for a wide range of Reynolds numbers. We then apply the method to a two-dimensional vertical axis turbine and to flows in mixed fluid-solid-porous media.

3.1 Flow past a 2D circular cylinder

There is an important literature about the classical benchmark of the 2D circular cylinder. This benchmark is covered by an important literature. A thorough survey of this subject can be found in Williamson (1996) [39].

Vortex methods using vorticity flux boundary conditions have allowed to obtain reference results for a wide range of Reynolds numbers [24]. Recently, the penalization-vortex method has been implemented on GPU processor. The accuracy and performance of this implementation against traditional CPU implementations has been tested on this benchmark in an explicit formulation of the penalization. We use here the same benchmark to illustrate the efficiency of the implicit formulation (equation (21)).

The computational domain and the geometrical setup are shown in figure 1, where D is a rectangle delimited by its boundaries Γ^D. The non dimensional diameter d of the circular cylinder and the free stream inlet velocity u_∞ are equal to 1. The whole computational domain is covered by a uniform Cartesian grid.

In this section, periodic boundary conditions on the box boundary Γ_D were prescribed for the system (18). A correction of the velocity field was performed at each time step in order to

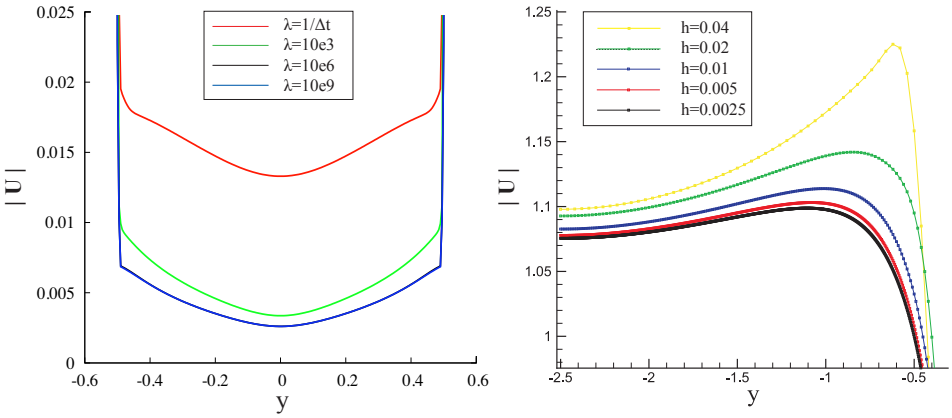

FIGURE 2 – Left picture : mean velocity magnitude profiles in a section across the center of the cylinder obtained with implicit penalization ($\lambda = 10^3, 10^6, 10^9$) and explicit penalization ($\lambda = 1/\Delta t$). Right picture : Grid refinement study for the axial velocity at $T = 3$ on a cross-section at $x = 1.5$ behind the cylinder.

satisfy free stream velocity $\mathbf{u}_\infty = (u_\infty, 0) = (1, 0)$ imposed at the inlet. In all cases the size of the computational box was chosen large enough so that the effect of these boundary conditions was found to be negligible.

First, we consider the case of an impulsively started cylinder flow with $\mathrm{Re} = 550$ and study the convergence of the method with respect to the penalization parameter and the grid-size. The left picture of figure 2 shows the mean velocity profiles inside the cylinder, averaged over the time window $[0, 3]$. The results corresponding to the implicit penalization scheme for three values of λ are compared to the profile obtained with the explicit formulation for a mesh size $h = 0.005$. The explicit formulation of (19) requires a maximum value of $\lambda = 1/\Delta t$ to guarantee stability. One can see from this experiment that, to obtain small values of the velocity inside the body, it is necessary to use larger value of λ, and therefore to implement the implicit scheme (21). One can also notice that velocity values inside the body remain in all cases much larger than $1/\lambda$, which implies that the formula (16) is not appropriate to evaluate the forces. The picture on the right side is a refinement study for a section located in the wake at $x = 1.5$ and a penalization parameter $\lambda = 10^{10}$ in the implicit formulation. It depicts the instantaneous velocity magnitude at time $T = 3$ for different grid sizes.

The first part of the study is related to the low Reynolds number analysis where the viscous effects are predominant. Following [29] the adimensional time-step Δt is determined by the condition $\Delta t/(h^2\ \mathrm{Re}) \sim O(1)$.

Various tests have been carried out by increasing the blockage ratio $1/L_y$, where L_y denotes the heigth of the computational box. The size of the computational domain was chosen such that the effects of the boundaries on the shedding frequencies were negligible. The subsequent simulations have been performed in a computational box with dimensions $[-7.5,\ 25]\times[-7.5,\ 7.5]$ with 3250×1500 grid points. This corresponds to a mesh size $h = 0.01$. The penalization was introduced using the implicit formulation (21) and the penalization parameter was set to $\lambda = 10^{10}$. Here, the flow regime is laminar, the solution is steady and stable for $\mathrm{Re} < \mathrm{Re}_{crit} = 49$ (see [39]). In figure 3, the streamlines for the steady solution at $\mathrm{Re} = 13.05$ are shown. On the left-hand side, a picture of an experimental visualization is reported (see [37]) and the equivalent

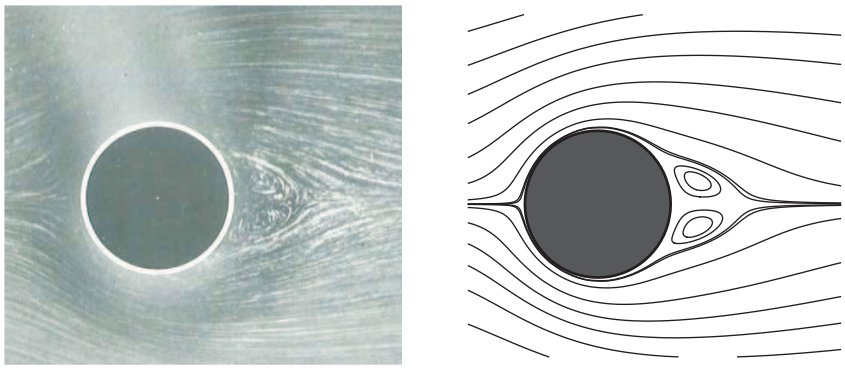

FIGURE 3 – Streamlines of flow past a circular cylinder at Re = 13.05. Experimental result obtained by M. van Dyke [37] (left). Numerical solution given by the present method (right).

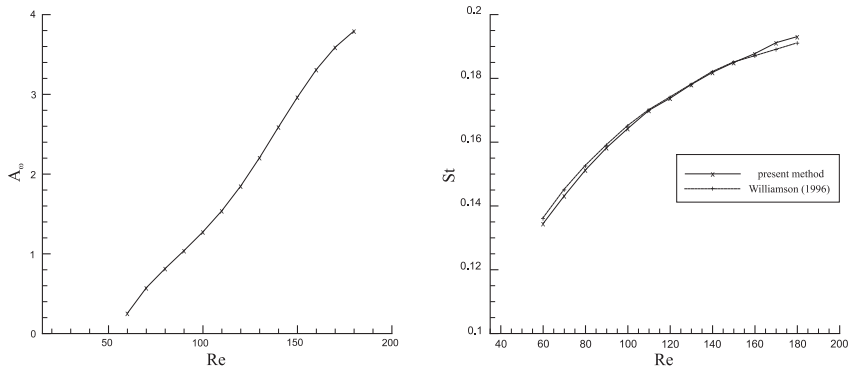

FIGURE 4 – Amplification factor A_ω curve (left). Strouhal-Reynolds curve (right).

frame computed by the present method is shown on the right-hand side. The figure shows a good qualitative agreement in the shape and size of the steady recirculation areas.

For larger Reynolds numbers, the flow regime is still laminar but the steady solution becomes unstable ($\mathrm{Re} > \mathrm{Re}_{crit}$). On the left-hand side picture of the figure 4, the amplitude A_ω of the fluctuation of the vorticity on a monitoring point $P = (2.5,\ 0.5)$ is plotted for various Reynolds numbers. For a flow regime close to the bifurcation point Re_{crit} ($\mathrm{Re} < 60$) the wake instabilities grow very slowly, so the oscillation study is started at Re = 60. Nevertheless, the exact critical Reynolds number is obtained with a linear extrapolation of the amplification factor curve. The right-hand side picture of the figure 4 shows the Strouhal number (given by the shedding frequency) as a function of the Reynolds number, obtained in our calculations and in the exprimental work ([39]). An estimation of the average relative error ϵ between the two curves yields $\epsilon \approx 0.6\%$.

The evaluation of forces has been carried out using the *momentum equation* (30). The mean values and the amplitudes of the fluctuations of drag and lift coefficients for flows at Re = 100 and Re = 200 are computed and given in Table 1. These results are very close to experimental and numerical data collected by Russell & Jane Wang [35] and Braza et al. [4].

To address a transitional case we focus now on an impulsively started flow at Re = 550 and compare our results to those of Ploumhans & Winckelmans [29] and Koumoutsakos & Leonard

	Re=100			Re=200		
Authors	$\bar{c_D}$	$\bar{c_L}$	S_t	$\bar{c_D}$	$\bar{c_L}$	S_t
Braza et al. [4]	1.36 ± 0.015	0 ± 0.25	0.160	1.40 ± 0.050	0 ± 0.75	0.190
Russel and Wang [35]	1.43 ± 0.009	0 ± 0.322	0.172	1.45 ± 0.036	0 ± 0.63	0.201
Present method	1.40 ± 0.010	0 ± 0.32	0.165	1.44 ± 0.05	0 ± 0.75	0.200

TABLE 1 – Comparison of drag coefficient, lift coefficient, and Strouhal number for flow past a cylinder at Re = 100 and Re = 200.

	Re=1000		
Authors	$\bar{c_D}$	$\bar{c_L}$	S_t
Apte et al. [2]	1.50	0 ± 1.36	0.238
Mittal et al. [26]	1.48 ± 0.21	0 ± 1.65	0.250
Present method	1.51 ± 0.23	0 ± 1.54	0.245

TABLE 2 – Comparison of drag coefficient, lift coefficient, and Strouhal number for flow past a cylinder at Re = 1000.

[24]. The time evolution of the drag coefficient is reported in figure 5(a). In our computations the the grid convergence in a computational domain $[-4,\ 8] \times [-5,\ 5]$ is achieved with parameters $h = 0.005$, $\Delta t = 0.005$ and $\lambda = 10^8$. The various results are in excellent agreement. Figure 6(a) depicts the vorticity isocontours which are very similar to the vorticity field presented by Ploumhans & Winckelmans [29] where $h = 6.03 \times 10^{-3}$.

The next simulation was performed at $Re = 1000$. At this regime, advection effects become predominant in the flow field. The boundary layer thickness decreases, requiring a finer grid. The mesh size is consequently set to $h = 0.0025$ in a computational domain $[-4,\ 8]\times[-5,\ 5]$ and the time step is set to $\Delta t = 0.003$. The non-dimensional time evolution of the drag coefficient is given in figure 5(b) and compared to the result in[24]. Table 2 shows the comparison of mean drag coefficient, amplitude fluctuation of lift coefficient and Strouhal number with other studies [2, 26] for long time simulations. All these comparisons confirm an excellent agreement between our results and the reference results in the literature.

For Re = 3000 the flow is unstable and the shedding generates complex vortex pairings (see [39]). In this case, grid convergence was obtained in our method for $\lambda = 10^8$, $h = 0.0025$ and $\Delta t = 0.0025$. Figure 5(c) shows again a very good agreement in the drag history between our results and those in [29] and [24]. In [29] h is about 0.002. Vortex contours in Figure 6(b) confirms this agreement.

The last simulation addresses the flow around the impulsively started cylinder at Re = 9500. In order to capture small spatial structures and the thin boundary layer, the grid size was reduced to the value $h = 0.00125$ in the same computational domain as the one used in the previous cases. The time step was set to 0.002 and $\lambda = 10^8$. The comparison of our results to those obtained by Rasmussen et al. [32] as well as Koumoutsakos & Leonard [24] is reported in figure 5(d). In [32] a multilevel vortex method was used with a minimal grid resolution corresponding to $h_{min} = 1/1024$. The discrepancy observed on Figure 5(d) at early times of the drag history indicates that the penalization method has difficulties to establish the strong initial vortex sheet on the body of the cylinder. For later times our results are in excellent agreement with [24, 32].

This validation study just performed for the 2D circular cylinder benchmark enables us to

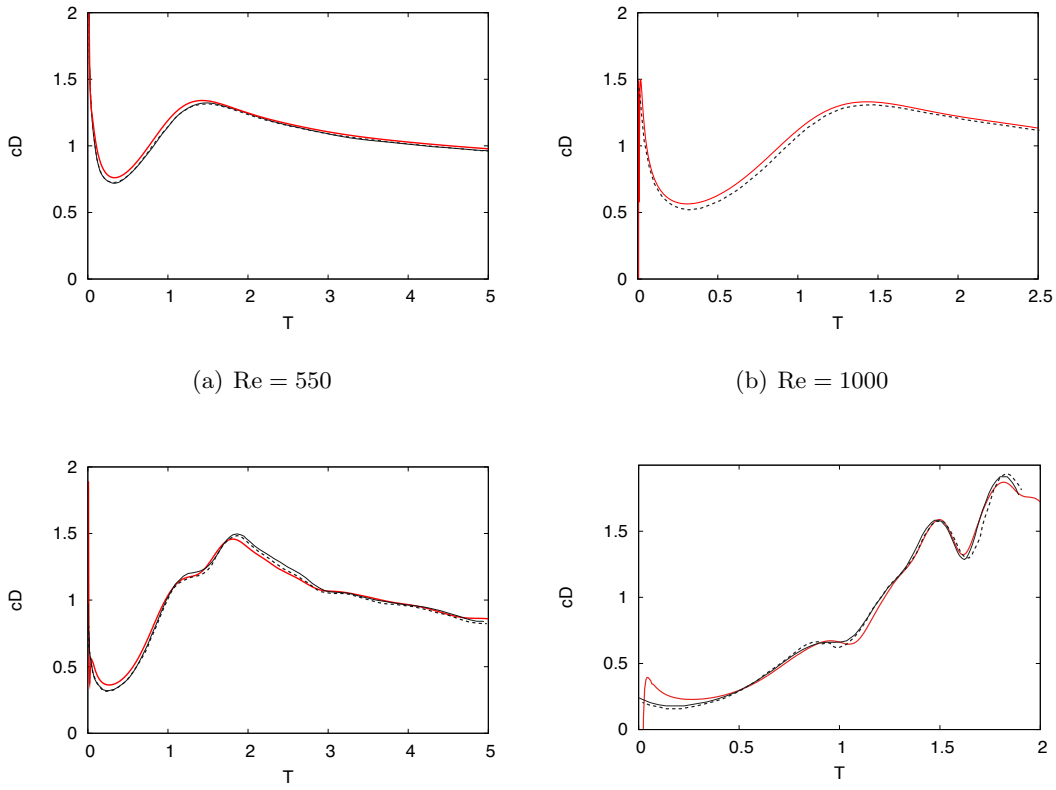

(a) Re = 550

(b) Re = 1000

(c) Re = 3000

(d) Re = 9500

FIGURE 5 – Drag evolution for Re = 550 (a), Re = 1000 (b), Re = 3000 (c) and Re = 9500 (d). Comparisons of present method (solid red line) with Koumoutsakos & Leonard [24] (dashed line). Solid black line are results from Ploumhans & Winckelmans [29] in (a), (b), (c) and from Rasmussen et al. [32] in (d).

determine the appropriate grid resolutions and time steps needed to obtain accurate results in the more challenging cases that will be considered next.

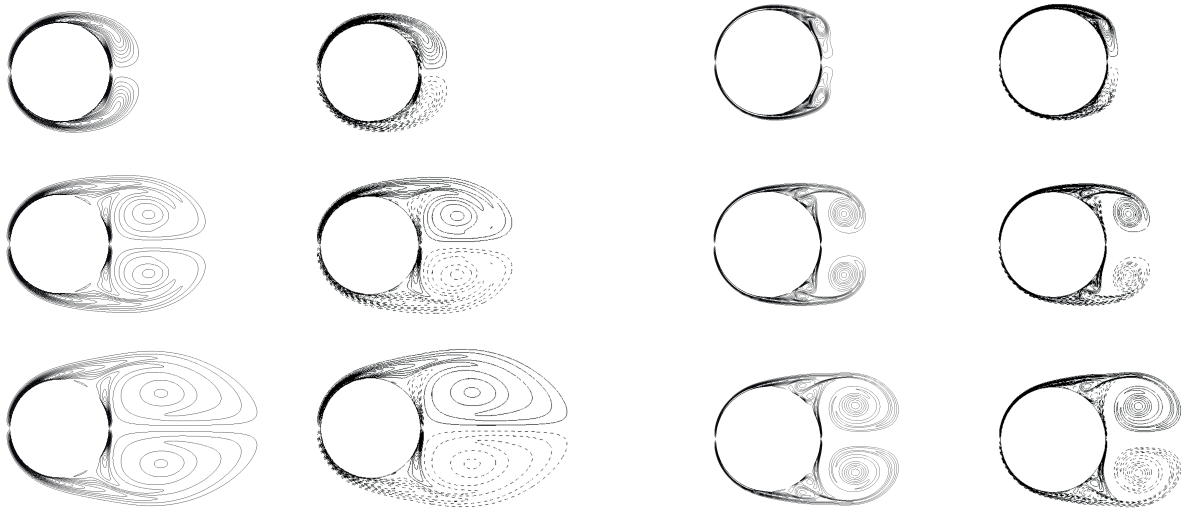

(a) Re = 550 (b) Re = 3000

FIGURE 6 – Comparison of vorticity isocontours for the impulsively started cylinder between present method (left columns) and Ploumhans & Winckelmans [29] (right columns) at (a) $T = 1$, 3, 5 at Re = 550 and (b) $T = 1$, 2, 3 at Re = 3000.

3.2 Flow past a moving two-dimensional vertical axis turbine

In this section, we apply the vortex penalization method to the two dimensional flow past a Vertical Axis Turbine (VAT). The VAT is rotating at a given velocity Ω and is immersed in a stream with a uniform far field velocity u_∞. The blade radius and the airfoil chord are denoted by R and c, respectively (Figure 7(a)).

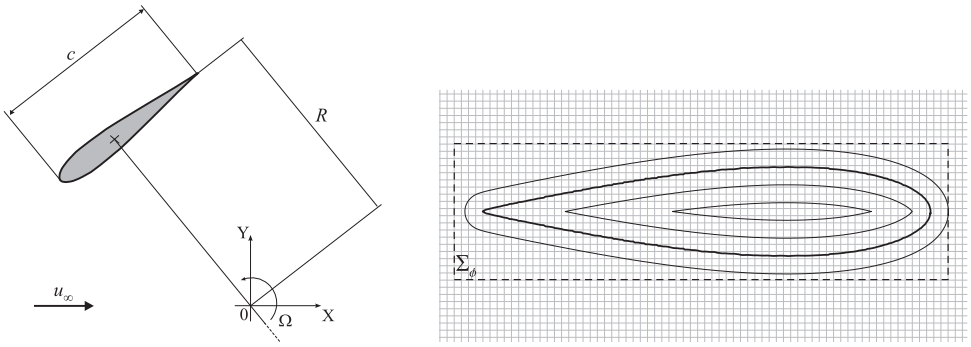

(a) (b)

FIGURE 7 – a) Geometrical setup of VAT. b) Distance function ϕ iso-contours ; the dashed rectangle Σ_ϕ is the support of ϕ.

The motion of a solid obstacle can be described with the vortex-penalization method as follows [15]. $S = S(t)$ is a moving multi-connected solid region. If one denotes by ϕ a level-set function which is negative inside S and positive outside, the characteristic function of S is defined by $\chi = \mathcal{H}(\phi)$, where $\mathcal{H}(\cdot)$ is a suitable step function. Moreover, in a rigid body motion, the level-set function has to satisfy

$$\frac{\partial \phi}{\partial t} + (\mathbf{u}_s \cdot \nabla)\, \phi = 0. \tag{34}$$

The above equation enables to evaluate the body trajectory. The equation (34) can be interpreted as a material derivative $D\phi/Dt = 0$, and the movement of the blade can be integrated using a Lagrangian method. The Figure 7(b), shows some levels of the function ϕ defining the airfoil on a grid 25 times larger than the one used for the simulation.

The blade section used in this vertical axis turbine is a symmetrical Kármán-Trefftz airfoil with a slightly smoothed trailing edge. The frame of reference is set on the rotation axis of the turbine and the computational domain is $D = [-6,\ 6] \times [-3.5,\ 3.5]$ with 3001×1751 grid points (corresponding to $h = 0.004$) and the penalization parameter $\lambda = 10^{10}$. The Poisson equation is solved using a finite differences-based solver with the following boundary conditions on the stream function ψ : on the upstream/downstream boundaries a Neumann condition is imposed, and on the horizontal boundaries a Dirichlet condition enforces the flow mass rate through the domain. The Reynolds number for a VAT can be defined choosing the blade section chord c as reference length and the maximum relative velocity $\mathbf{u}_{rel}^{max}$ as reference velocity, where this velocity is given by $\mathbf{u}_{rel}^{max} = |u_\infty| + |\Omega R|$. For a realistic simulation of a medium/small wind or water turbine it is located in the range of $10^4 - 10^6$. The flow is transitional and is dominated by convective phenomena. In this section two values of the Reynolds numbers, $\mathrm{Re} = 1000$ and $\mathrm{Re} = 10000$, are considered. This bench study mainly aims to highlight the great capability of the present method to supply realistic results for moving bodies with unfitted boundaries and

the grid resolution handled here is convenient to confirm the qualitative physical behaviour of computations.

For the Reynolds number Re = 1000, a wind turbine with a blade section chord $c = 0.2$ m, radius $R = 0.3$ m, rotating speed $\Omega = 0.185$ rad/s and immersed in a stream with $u_\infty = 0.025$ m/s is considered (where $\nu_{air} = 1.6\ 10^{-5}$ m^2/s at 20 Celsius degrees). For this Reynolds number, which corresponds to a low transitional flow with viscous effects, the time step is taken as $\Delta t = 0.001$. A higher Reynolds number for a wind turbine operating at low-wind speed is studied by considering this VAT geometry with the working conditions $\Omega = 1.85$ rad/s and $u_\infty = 0.25$ m/s. The corresponding Reynolds number is Re = 10000 and the integration time step is chosen to be $\Delta t = 0.0002$. On Figures 8(a) and 8(b) instantaneous vorticity isolines for different rotating times of the blades at Re = 1000 and Re = 10000 are respectively plotted. The varying incidence of the velocity occurring at each blade generates separation and vortex shedding ; as the figures show, the flow is highly unsteady and the blade strongly interacts with the wake. The flow for Re = 1000 generates an almost regular Von-Kármán-like wake with large structures. By contrast, the vortex shedding for the Re = 10000 becomes very quickly unsteady where small high frequency vortical structures interact with each other before being transported downstream.

A complementary description of the flow around the turbine is given by the time averaged streamlines shown on Figures 9(a) and 9(b), for a fully developed wake at Re = 1000 and Re = 10000. Here, the frame of reference is centered on the axis of the turbine and rotates together with the blades. For the lower Reynolds number Re = 1000 the average is computed for a simulation time of $\approx$ 650s, which corresponds to $\approx$ 19 loops of the blade. As the Figure 9(a) shows, for this flow the recirculation zones (one for each blade) are concentrated between the rotation axis and the inner surface of the blade. For the higher Reynolds number Re = 10000, the mean flow is computed for a simulation time of $\approx$ 65s, which still corresponds to $\approx$ 19 cycles. In this case, for each blade three recirculating areas can be identified, as in Figure 9(b) : two zones are close to the airfoil (outer and inner surfaces) and the third region is the average in time of the wake generated from the trailing edge of each blade due to complex vortex interactions.

Finally, we study the time evolution of the enstrophy ϵ and the number of vortex particles in order to better analyze the properties of these two flow regimes. The enstrophy is a quantity that measures the dissipation of energy in terms of kinetic energy. In a 2D flow field the enstrophy is given by $Z = \int_D |\omega|^2 d\sigma$, where D is the computational domain. In figures 10(a) and 10(b) the comparison between the time history of the enstrophy and the number of particles is shown for Re = 1000 and Re = 10000 respectively. As the figure 10(a) shows, the amplitude of the oscillations remains quite small compared to the Re = 10000 regime (Fig. 10(b)), where the frequency of the shedding appears through large oscillations. The figures show the high correlation between the time evolution of the enstrophy and the number of particles.

In the present cases the flow regime is characterized by unsteady separations generated by the periodical interaction of the wake with the blades. For Re = 1000, we notice that the principal vortex shedding frequency roughly corresponds to 2Ω, that is twice the angular velocity of the two-bladed VAT. For Re = 10000, different shedding frequencies can be distinguished from the rotational frequency of the blade. The investigation on the shedding frequencies is meaningful because it allows to relate the interaction of the vortex wake with the structure of the turbine. If some vortex shedding frequencies match the proper frequencies of the turbine, the structure can resonate with a self-sustained motion and the turbine is liable to aeroelastic phenomena. To evaluate the principal frequencies of vortex shedding we performed a discrete Fourier analysis of the enstrophy signal. In figures 11(a) and 11(b) the spectra of the enstrophy

versus the frequency of the signal are presented, where $A_{enstrophy}$ is the amplitude of the enstrophy and ω_i/Ω is the nondimensional discrete frequency of the signal. The spectra does not report the mean value corresponding to the first coefficient $i = 0$ of the Fourier series. To avoid the effect of the initial transient stage, the Fourier analysis was applied on the signals after the first three cycles of the turbine.

In figure 11(a) the shedding principal harmonic at 2 times the angular velocity of the turbine is confirmed : the wake interacts with a blade two times for each cycle of the turbine. Further couplings with the principal frequency can be identified at 4, 6, 8. Some high energy contributions are visible at frequencies lower than 2. A reason may be that the flow is not fully developed and did not achieve a statistical steady state yet.

In figure 11(b) the spectrum exhibits shedding frequencies at 2 and 4 times the angular velocity. Since at this regime the flow is turbulent, the enstrophy signal is noisy and is characterized by random peaks at low frequency (Fig. 10(b)). Higher couplings with the principal rotational frequency are not visible by the spectrum, because the energy is transferred from the large geometrical scale to the smaller Kolmogorov scale. The large energetic contribution occurring at frequencies lower than 2 probably means that the flow is not yet fully developed.

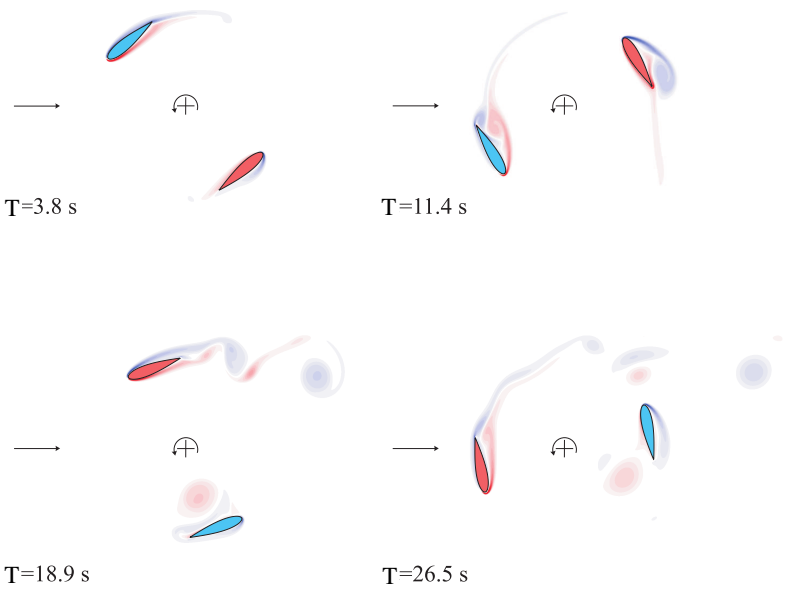

(a) Re = 1000

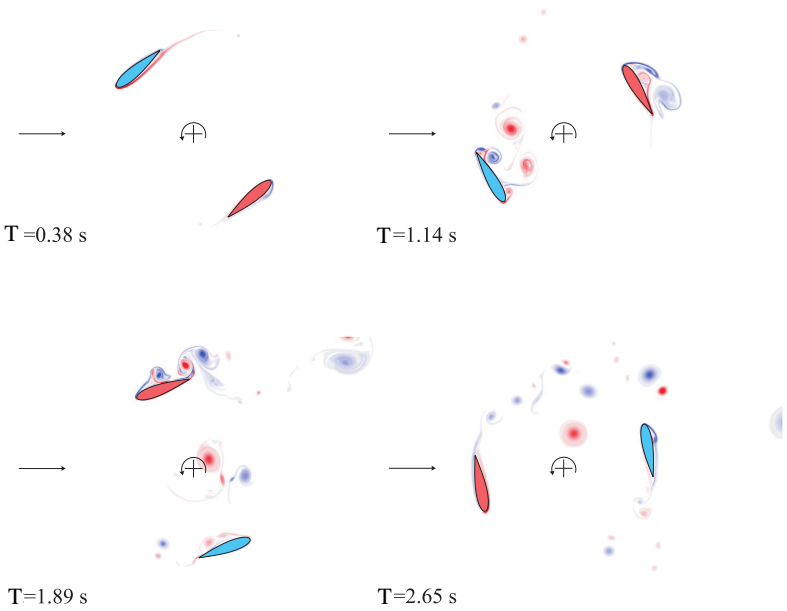

(b) Re = 10000

FIGURE 8 – Iso-vorticity lines of the wake past the VAT at Re = 1000 (a) and at Re = 10000 (b). Snapshots respectively at times $T = 3.8$s, 11.4s, 18.9s, 26.5s and $T = 0.38$s, 1.14s, 1.89s, 2.65s.

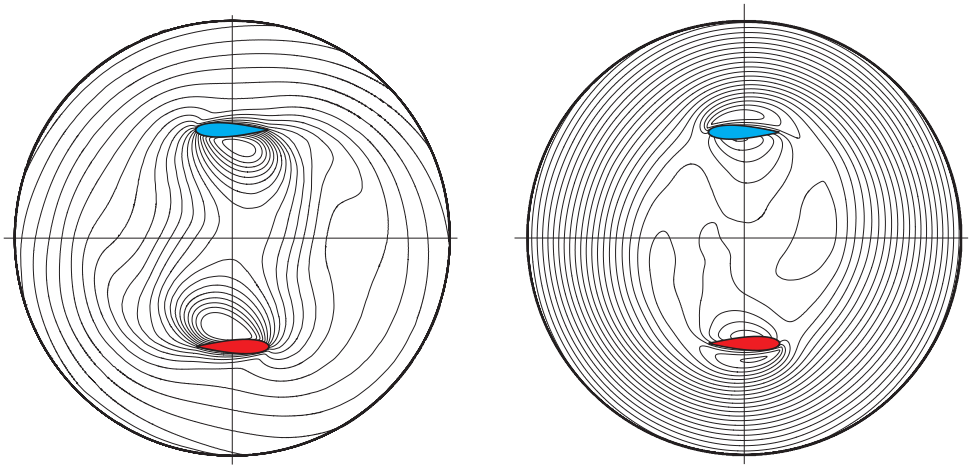

(a) (b)

FIGURE 9 – Averaged-in-time streamlines for the VAT at Re = 1000 (a) and at Re = 10000 (b). The iso-lines are represented in the relative frame of reference.

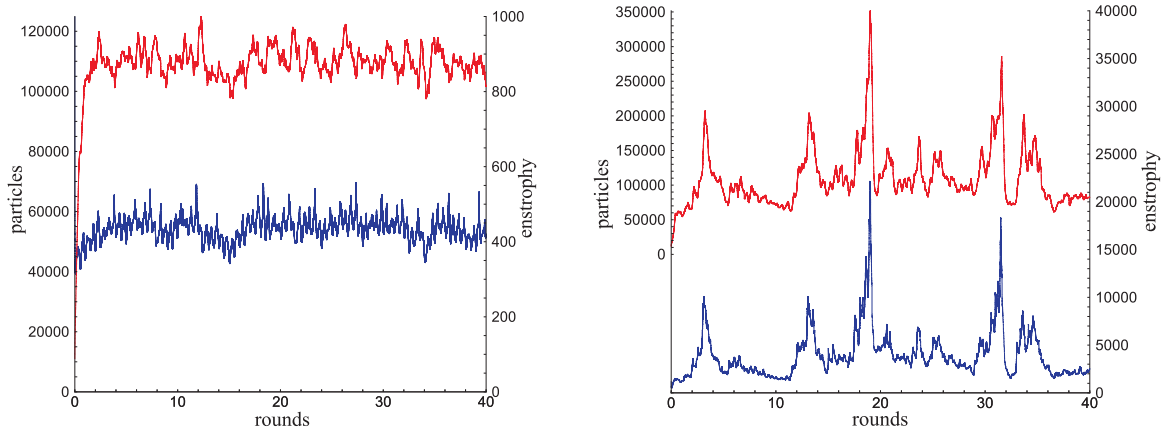

(a) (b)

FIGURE 10 – Time history of the dimensionless enstrophy Z (blue) and the number of vortex particles (red) for Re = 1000 (a) and Re = 10000 (b). The axis of the abscissas represents the number of the cycles performed by the turbine.

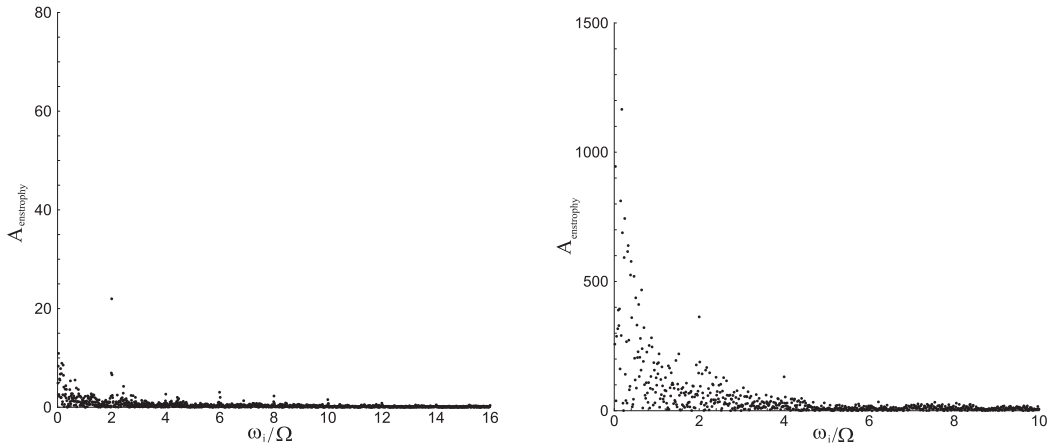

(a) (b)

FIGURE 11 – Frequency spectrum of the enstrophy signal computed for Re = 1000 (a) and Re = 10000 (b). The horizontal axis reports the discrete frequency ω_i divided by the angular velocity Ω of the turbine.

4 Applications to solid-porous-fluid media and flow control

This section is devoted to the study of flows in solid-porous-fluid media. It illustrates the efficiency of the vortex penalization method to solve such problems.

4.1 Modeling and numerical setup

Following [10], we consider a solid body surrounded by a porous layer and immersed in an incompressible fluid. In such a system, on can identify five different flow regimes corresponding to different regions in the fluid. A first region is the boundary layer inside the porous medium, close to the solid wall. This region is very thin compared to the second region which is characterized by the homogeneous porous flow with Darcy velocity (regions numbered 1 and 2 in figure 12(left)). In the vicinity of the porous-fluid interface, two transient layers can be recognized (numbered 3 and 4 in figure 12(left)). The first one corresponds to the porous layer velocity increasing to reach a value $\mathbf{u}_i$ at the interface, and the second one to the fluid boundary layer leading to the free external flow. The fluid boundary layer size is then determined by $\mathbf{u}_0 - \mathbf{u}_i$ where $\mathbf{u}_0$ denotes the velocity of the main fluid flow (numbered 5 in figure 12(left)). The goal is thus to compute the flow simultaneously in the porous medium, the fluid region and at the interface between the two media. Several approaches have already been proposed to handle this problem. The first one, which is mainly used to model flows past a solid with permeable walls [20, 22], avoids to solve the porous flow by enforcing appropriate porous-fluid boundary conditions [3]. This method neglects the porous medium physics and does not permit to have an overall view of the problem. A second approach considers that the porous flow has to be accurately computed, and solves the governing equations in each region coupling the Darcy equations and the Navier-Stokes equations with an appropriate condition at the interface [5, 21]. This approach is very difficult to handle especially because of the requirement of this appropriate boundary condition. The method presented here, based on the vortex-penalization technique, considerably simplifies the task since a unique equation is used for the whole domain and enables to accurately model each of the different regions by varying the value of the dimensionless penalization factor λ. In 2 dimensions, the penalized vorticity equation reads :

$$\frac{\partial \omega}{\partial t} + (\mathbf{u}.\nabla)\omega = \frac{1}{\mathrm{Re}}\Delta\omega + \nabla \times [\lambda\ \chi_S(\mathbf{u}_s - \mathbf{u})]. \tag{35}$$

We recall that λ essentially depends, in the inverse proportion, on the physical intrinsic permeability of the medium k which directly derives from the Darcy law (equation (7)). Varying the λ value thus directly characterizes the different media.

Modeling the physics of three different regions enables one to deal with engineering problems involving porous media. In the following, this approach is validated for a simple but informative passive flow control problem. It was already used in [9, 8] with finite-difference methods for pipe or square geometries. Here, the solid-porous-fluid configuration is applied to cover a semi-circular cylinder geometry with a porous coating. The porous coating is applied on the obstacle external surface in order to modify the vorticity generation of the boundary layer and the vortex shedding. The presence of a porous medium at the solid-fluid interface indeed imposes a kind of mixed boundary condition intermediate between the no-slip and the slip one on the solid boundary [12]. As a result, the shear forces are reduced and the flow dynamics is smoothed [8, 9, 10, 7]. This control technique, which allows to keep the obstacle geometry unchanged, is expected to reduce drag forces and vortex induced vibrations, thereby improving

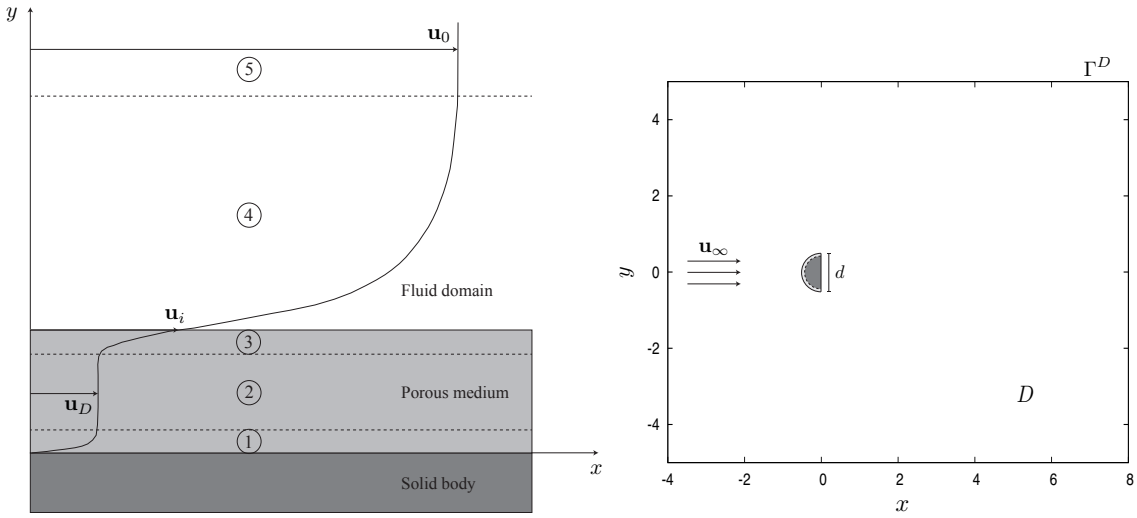

FIGURE 12 – Velocity profile in the vicinity of a porous medium (left). Computational domain for flow control past semi-circular cylinder (right)

the aerodynamic properties of the obstacle. The semi-circular cylinder can be considered as a simplified section of an outside rear-view mirror of a vehicle. The mirrors, due to their spanwise location, indeed generate a non-negligible wake which interferes with the flow past vehicle sides. This provides a good motivation to perform flow control past such obstacles. As it was shown in [34, 6], a flow past a square back obstacle is not dominated by longitudinal vortical structures, therefore a preliminary two-dimensional study can be useful to supply information on general trends for a control. However, the flow is three-dimensional and this 2D study will be complemented by 3D computations.

In the following, the semi-circular cylinder has a total dimensionless diameter of $d = 1$ including a porous layer of thickness $\tau = 0.1$ The backward face of the obstacle is centered at the point $(0, 0)$ (see Figure 12(right)). We first perform a convergence study of the method applied to flow past a solid semi-circular cylinder, then present a λ-parametric study allowing to determine the most efficient permeabilities in terms of flow control. We will consider flows both at transitional ($\mathrm{Re} = 550$) and highly transitional ($\mathrm{Re} = 3000$) regimes.

4.2 Grid convergence

We consider in this section the vortex-penalization method for flow past a solid semi-circular cylinder at $\mathrm{Re} = 550$ and $\mathrm{Re} = 3000$. Grid convergence is studied on three grid levels. For $\mathrm{Re} = 550$ the three consecutive mesh sizes are : $h = 0.01$, $h = 0.005$ and $h = 0.0025$ in the computational domain $D = [-4,\ 8] \times [-4,\ 4]$. For $\mathrm{Re} = 3000$ as the boundary layer is thiner, we perform the convergence study with three finer mesh sizes, respectively $h = 0.005$, $h = 0.0025$ and $h = 0.00125$. The simulations are carried out in a smaller domain $D = [-2.5,\ 5] \times [-3,\ 3]$ in order to reduce the computational cost induced by the finest grid. Mean drag and enstrophy values are reported in Table 3. At $\mathrm{Re} = 550$, on the basis of these results, one can consider that the grid convergence is achieved for $h = 0.005$ with $\Delta t = 0.025$. At $\mathrm{Re} = 3000$ grid convergence is achieved with $h = 0.0025$ and $h = 0.00125$, which leads us to choose $h = 0.0025$ and $\Delta t = 0.002$ for the coming simulations. Let us emphasize the interest of the vortex methods

which enables here to handle a highly transitional regime using a relatively large time step compared to classical Eulerian methods.

	Re = 550		Re = 3000	
Grid	C_D	Z	C_D	Z
$h = 0.01$	1.49	122	-	-
$h = 0.005$	1.91	158	1.89	313
$h = 0.0025$	1.98	161	1.94	292
$h = 0.00125$	-	-	1.96	280

TABLE 3 – Mean values of drag coefficient C_D and enstrophy Z for flow past a semi-circular cylinder at Re = 550 and Re = 3000.

4.3 Parametric study with respect to the penalization parameter λ

In this section we study the influence of the porous layer permeability on the flow behavior and the efficiency of such a passive control. This parametric study is performed at Re = 550 and Re = 3000 with four different values of the porous permeability inside the layer, namely $\lambda = 1$ (high permeability), 10, 10^2, 10^3 (low permeability). Results are compared the results corresponding to the solid ($\lambda = 10^8$) and fluid ($\lambda = 0$) cases. In all cases, the thickness of the coating is set to ten percent of the diameter : $\tau = 0.1$ (see Figure 13). According to the grid convergence performed in the previous section (Table 3), the numerical simulations are performed on a 2400×2000 grid (corresponding to $h = 0.005$) for Re = 550 and on a 4800×4000 grid (corresponding to $h = 0.0025$) for Re = 3000 in a computational domain $D = [-4,\ 8] \times [-5,\ 5]$ (see Figure 12(right)).

In order to analyze the effects of our control approach we compare global flow quantities like the drag force ($\mathcal{F}_x$), computed according to the *momentum equation* (30) and the enstrophy (Z) allowing to measure the dissipation effects in the flow as well as the delay of transition to turbulence. Note that in this study we consider drag forces instead of drag coefficients since the C_D formula (33) involves the diameter d of the obstacle which is not clearly defined because of the porous coating.

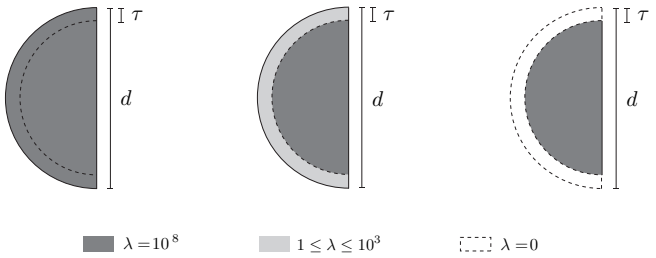

FIGURE 13 – (left) Solid/uncontrolled case, (center) Porous case, (right) Fluid case.

As can be seen in figure 14, which represents the time history of the global flow quantities at Re = 550, the value $\lambda = 1$ inside the layer clearly appears to provide the best solution in terms of flow regularization. Indeed, the mean value of the drag force reaches for $\lambda = 1$ a minimum value, close to that of the fluid case, with a drag reduction of about 30% compared to uncontrolled case (Table 4). For all the other values of porous λ, the drag reduction effects are small or even negative (Table 4). The enstrophy evolution (Figure 14(b)) shows a progressive reduction of the dissipation effects and the delay of transition to turbulence as the value of λ decreases. Furthermore, we note that the result obtained with $\lambda = 1$ is even better than the one of fluid case and represents an improvement of nearly 40% compared to uncontrolled case (Table 4). The benefits induced by the presence of a highly porous layer are also highlighted in figures 16 and 18 respectively depicting the mean velocity and mean vorticity fields. As already emphasized in the literature [6, 7], the main source of drag forces for bluff bodies with square back is the low pressure recirculation zone in the near wake of the vertical wall. With $\lambda = 1$, the near wake structures are smaller and the back recirculation zone is drastically reduced (Figure 18). Moreover, the vortices swirl with a low velocity (Figure 16) and the structure of the global and near wake resembles the one of the fluid case. This feature explains the important drag reduction observed in figure 14(a). On the contrary, the flow behavior obtained with $\lambda = 10$ looks very similar to the one of the uncontrolled case with an important transversal extent of

	Re = 550		Re = 3000	
Cases	$\bar{\mathcal{F}}_x$	$\bar{Z}$	$\bar{\mathcal{F}}_x$	$\bar{Z}$
uncontrolled case	0.957	158.4	0.926	334.2
porous case $\lambda = 1000$	0.957 (-0%)	154.0 (-3%)	0.936 (-1%)	325.8 (-2%)
porous case $\lambda = 100$	0.968 (+1.1%)	143.3 (-10%)	0.873 (-6%)	270.0 (-19%)
porous case $\lambda = 10$	0.970 (+1.4%)	114.4 (-28%)	1.054 (+14%)	248.8 (-26%)
porous case $\lambda = 1$	0.695 (-29%)	97.5 (-38%)	0.870 (-6%)	236.7 (-29%)
fluid case	0.640	110.9	0.880	319.3

TABLE 4 – Reduction effects in terms of mean drag force and mean enstrophy brought by the different layer permeabilities in comparison to the uncontrolled case at Re = 550 and Re = 3000.

the wake (Figure 18) and high velocities in the flow compared to the uncontrolled case. This confirms the results given in Table 4 and leads us to conclude that this value of λ is not suitable at this regime for our control approach.

At Re = 3000 the best solution for global flow regularization is also achieved setting the λ parameter to 1 inside the porous coating. This configuration leads to a drag and enstrophy reduction of 6% and about 30%, respectively, compared to the uncontrolled case (Figure 15 and Table 4). It leads to a significant regularization of the global flow field characterized by a symmetric, thin and regular wake, and to smaller velocity gradients and vorticity values in the vicinity of the detachment points and the recirculation zone (Figure 17 and 19). Moreover this study emphasizes a phenomenon which already starts to emerge at Re = 550 and which concerns the flow behavior observed when $\lambda = 10$ inside the layer. In this case, the flow field experiences a high resistance inside the intermediate permeable medium, increasing the mean drag force by 14% compared to the uncontrolled case (Table 4). Figure 17 also confirms the negative effects of this layer permeability at such a regime, showing a chaotic wake with high velocity gradients. In conclusion, all these results indicate that at Re = 3000 the control should also be implemented with the high permeability coefficient $\lambda = 1$.

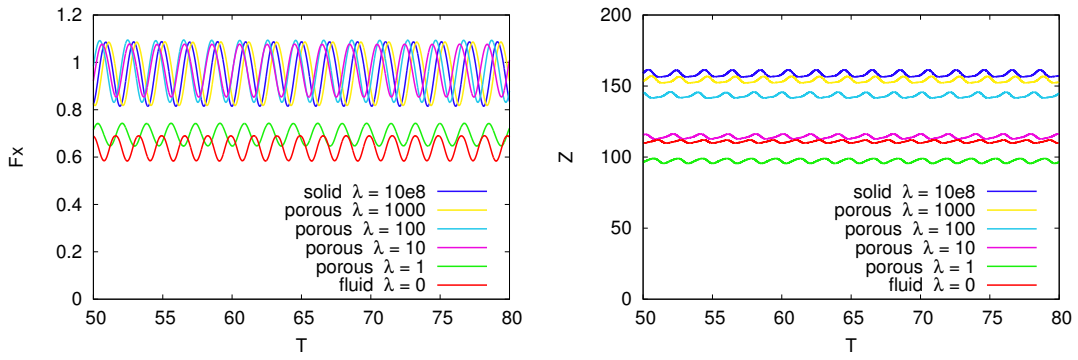

(a) Dimensionless time history of drag force ($\mathcal{F}_x$) (b) Dimensionless time history of enstrophy (Z)

FIGURE 14 – Effects of various layer permeabilities on the global flow quantities related to flow past a semi-circular cylinder at Re = 550 with $\tau = 0.1$.

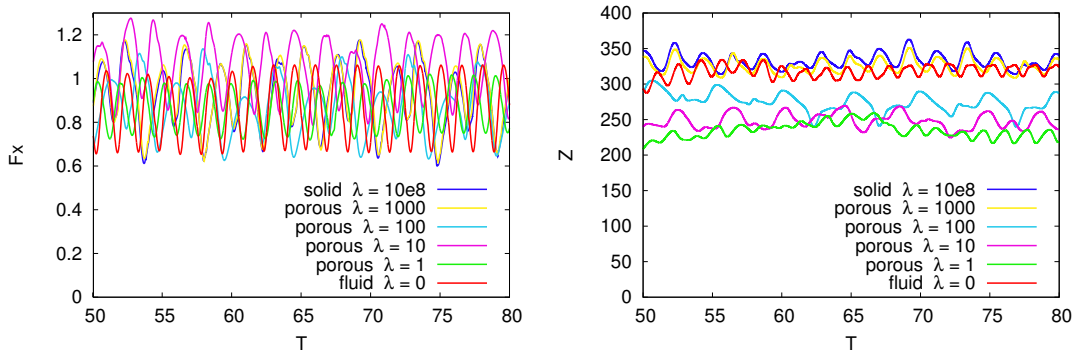

(a) Dimensionless time history of drag force ($\mathcal{F}_x$) (b) Dimensionless time history of enstrophy (Z)

FIGURE 15 – Effects of various layer permeabilities on the global flow quantities related to flow past a semi-circular cylinder at Re = 3000 with $\tau = 0.1$.

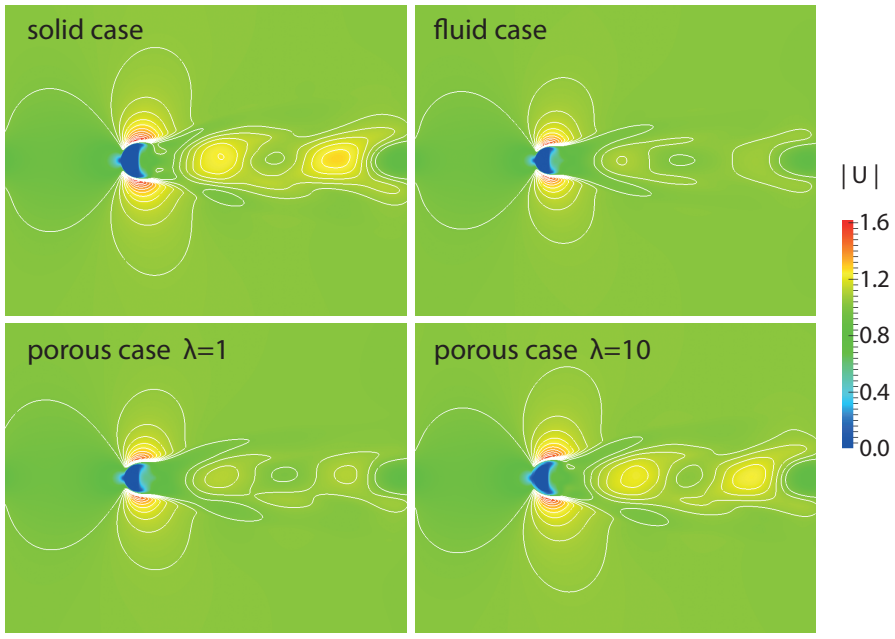

FIGURE 16 – Fields and isolines of mean velocity magnitude for the flow past a semi-circular cylinder at Re = 550.

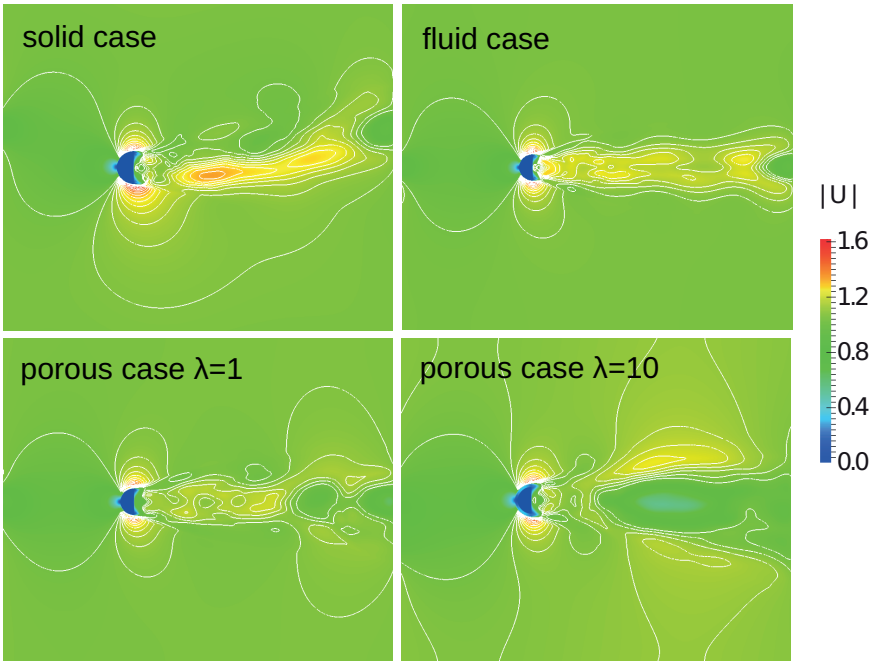

FIGURE 17 – Isolines of mean velocity magnitude for the flow past a semi-circular cylinder at Re = 3000.

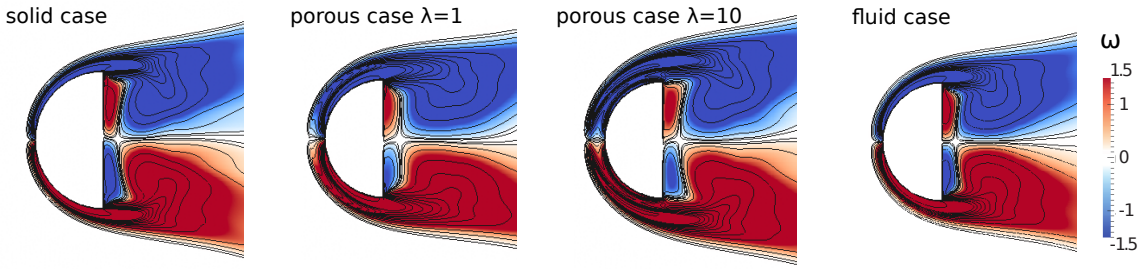

FIGURE 18 – Zoom of the mean vorticity fields and isolines for the flow past a semi-circular cylinder at Re = 550.

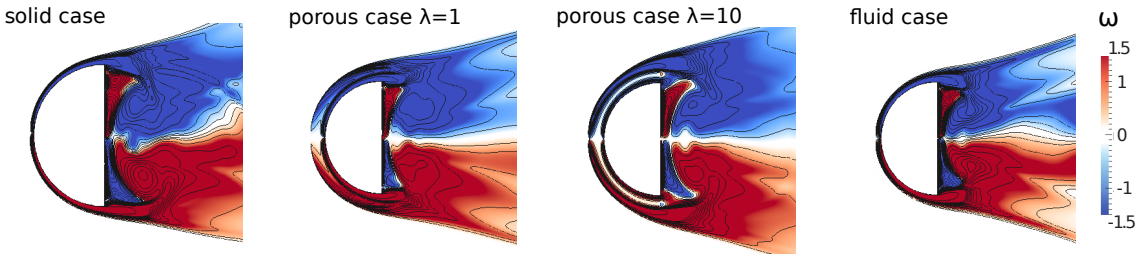

FIGURE 19 – Zoom of the mean vorticity fields and isolines for the flow past a semi-circular cylinder at Re = 3000.

5 Conclusion

In this paper a method combining penalization, vorticity formulation and particle discretization was described and applied to complex fluid-solid configurations. The penalization approach greatly simplifies the implementation of vortex particle methods to handle accurately the no-slip boundary conditions. Moreover, the penalization method enables to consider the governing equations in the whole computational domain allowing the use of simple cartesian grids and fast Poisson solvers to compute velocity fields. After a detailed validation on the circular cylinder benchmark, a the first application to moderate and high Reynolds flows around a moving vertical axis turbine was presented. The results showed the efficiency of this hybrid vortex immersed boundary method to realistically model flows past moving obstacles. The second application illustrated the capability of the method to handle solid-fluid-porous media. The distinction between the three different media is indeed performed by varying the value of the penalization parameter without prescribing a boundary condition at the solid boundary or at the porous-fluid interface. An application to passive flow control past a semi-circular cylinder was performed at transitional and highly transitional regimes, consisting in adding a porous sheath on the obstacle surface in order to smooth the flow dynamics. The presence of a porous layer at the solid-fluid interface is responsible for a decrease of the shear forces and the vorticity generation of the boundary layer, leading to significant wake stabilization and drag reduction. This paper thus confirms the versatility of the method for complex flow problems.

Références

[1] P. Angot, C. H. Bruneau, and P. Fabrie. A penalization method to take into account obstacles in incompressible viscous flows. *Numerische Mathematik*, 81 :497–520, 1999.

[2] S. V. Apte, M. Martin, and N. A. Patankar. A numerical method for fully resolved simulation (frs) of rigid particle-flow interactions in complex flows. *J. Comput. Phys.*, 228 :2712–2738, 2008.

[3] G. D. Beavers and D. D. Joseph. Boundary conditons at a naturally permeable wall. *J. Fluid Mech.*, 30 :197–207, 1967.

[4] M. Braza, P. Chassaing, and H. H. Minh. Numerical study and physical analysis of the pressure and velocity fields in the near wake of a circular cylinder. *J. Fluid Mech.*, 165 :79–130, 1986.

[5] W. P. Breugem, B. J. Boersma, and R. E. Uittenbogaard. The laminar boundary layer over a permeable wall. *Transp. Porous Med.*, 59 :267–300, 2005.

[6] C. H. Bruneau, E. Creusé, D. Depeyras, P. Gilliéron, and I. Mortazavi. Coupling active and passive techniques to control the flow past the square back ahmed body. *Comput. Fluids*, 38 :1875–1892, 2010.

[7] C. H. Bruneau, P. Gilliéron, and I. Mortazavi. Passive control around a two-dimensional square back ahmed body using porous media. *J. Fluids Engineering*, 130, 2008.

[8] C. H. Bruneau and I. Mortazavi. Passive control of the flow around a square cylinder using porous media. *Int. J. Numer. Meth. Fluids*, 46 :415–433, 2004.

[9] C. H. Bruneau and I. Mortazavi. Control of vortex shedding around a pipe section using a porous sheat. *J. Offshore and Polar Eng.*, 16, 2006.

[10] C. H. Bruneau and I. Mortazavi. Numerical modelling and passive flow control using porous media. *Comput. Fluids*, 37 :488–498, 2008.

[11] J. P. Caltagirone. Sur l'intéraction fluide-milieu poreux : Application au calcul des efforts exercés sur un obstacle par un fluide visqueux. *C. R. Acad. Sci. Paris*, 318, 1994.

[12] G. Carbou. Brinkmann model and double penalization method for the flow around a porous thin layer. *J. Math. Fluid Mech.*, 10 :126–158, 2008.

[13] A. J. Chorin. Numerical study of slighly viscous flow. *J. Fluid Mech.*, 57 :785–796, 1973.

[14] A. J. Chorin. Vortex sheet approximation of boundary layers. *J. Comput. Phys.*, 27 :428–442, 1978.

[15] M. Coquerelle and G. H. Cottet. A vortex level-set method for the two-way coupling of an incompressible fluid with colliding rigid bodies. *J. Comput. Phys.*, 227 :9121–9137, 2008.

[16] G. H. Cottet and P. D. Koumoutsakos. *Vortex Methods - Theory and Practice*. Cambridge University Press, 2000.

[17] G.-H. Cottet and P. Poncet. Advances in direct numerical simulation of 3D wall-bounded flows by vortex-in-cell methods. *J. Comput. Phys.*, 193 :136–158, 2004.

[18] G.H. Cottet, M. Etancelin, F. Perignon, and C. Picard. Semi-lagrangian particles for transport equations : numerical analysis and implementation issues. Technical report, 2013. submitted.

[19] E. Creusé, A. Giovannini, and I. Mortazavi. Vortex simulation of active control strategies for transitional backward-facing step flows. *Computers & Fluids*, 38 :1348–1360, 2009.

[20] S. Hahn, J. Je, and H. Choi. Direct numerical simulation of turbulent channel flow with permeable walls. *J. Fluid Mech.*, 450 :259–285, 2002.

[21] N. S. Hanspal, A. N. Waghode, V. Nassehi, and R. J. Wakeman. Numerical analysis of coupled stokes/darcy flows in industrial filtrations. *Transp. Porous Med.*, 64 :73–101, 2006.

[22] J. Jimenez, M. Uhlmann, A. Pinelli, and G. Kawahara. Turbulent shear flow over active and passive porous surfaces. *J. Fluid Mech.*, 442 :89–117, 2001.

[23] N. Kevlahan and J. M. Ghidaglia. Computation of turbulent flow past an array of cylinders using a spectral method with brinkman penalization. *Eur. J. Mech.*, B 20 :333–350, 2001.

[24] P. Koumoustakos and A. Leonard. High-resolution simulations of the flow around an impulsively started cylinder using vortex methods. *J. Fluid Mech.*, 296 :1–38, 1995.

[25] P. Koumoutsakos, A. Leonard, and F. Pépin. Boundary conditions for viscous vortex methods. *J. Comput. Phys.*, 113(1) :52–61, 1994.

[26] S. Mittal and V. Kumar. Flow-induced vibrations of a light circular cylinder at reynolds numbers 1000 to 10000. *Journal of Sound and Vibration*, 245 :923–946, 2001.

[27] D. A. Nield and A. Bejan. *Convection in Porous Media*. Springer, 1999.

[28] F. Noca, D. Shiels, and D. Jeon. A comparison of methods for evaluating time-dependent fluid dynamic forces on bodies, using only velocity fields and their derivatives. *J. Fluids Struct.*, 13 :551–578, 1999.

[29] P. Ploumhans and G. S. Winckelmans. Vortex methods for high-resolution simulations of viscous flow past bluff bodies of general geometry. *J. Comput. Phys.*, 165 :354–406, 2000.

[30] P. Ploumhans, G. S. Winckelmans, J. K. Salmon, A. Leonard, and M. S. Warren. Vortex methods for direct numerical simulation of three-dimensional bluff body flows : Applications to the sphere at $Re = 300$, 500 and 1000. *J. Comput. Phys.*, 178 :427–463, 2002.

[31] P. Poncet. Topological aspects of the three-dimensional wake behind rotary oscillating circular cylinder. *J. Fluid Mech.*, 517 :27–53, 2004.

[32] J. T. Rasmussen, G. H. Cottet, and J. H. Walther. A multiresolution remeshed vortex-in-cell algorithm using patches. *J. Comput. Phys.*, 230 :6742–6755, 2011.

[33] D. Rossinelli, M. Bergdorf, G.-H. Cottet, and P. Koumoutsakos. Gpu accelerated simulations of bluff body flows using vortex particle methods. *J. Comput. Phys.*, 229 :3316–3333, 2010.

[34] M. Rouméas, P. Gilliéron, and A. Kourta. Analysis and control of the near-wake flow over a square-back geometry. *Comput. Fluids*, 38 :60–70, 2009.

[35] D. Russell and Z. J. Wang. A cartesian grid method for modeling multiple moving objects in 2D incompressible viscous flow. *J. Comput. Phys.*, 191 :177–205, 2003.

[36] P. G. Saffman. *Vortex Dynamics*. Cambridge University Press, 1992.

[37] M. van Dyke. *An Album of Fluid Motion*. Stanford : The Parabolic Press, 1982.

[38] S. Whitaker. *The Method of Volume Averaging*. Kluwer : Dordercht, 1999.

[39] C. H. K. Williamson. Vortex dynamics in the cylinder wake. *Annu. Rev. Fluid. Mech.*, 28 :477–539, 1996.